PAPER • OPEN ACCESS

Microstructure of additive manufactured materials for plasma-facing components of future fusion reactors

View the article online for updates and enhancements.

Microstructure of additive manufactured materials for plasma-facing components of future fusion reactors

D A H Wartacz[1], H Becker[1,2], S Antusch[3], N Ordás[4], C Gundlach[5], O V Mishin[1] and W Pantleon[1]*

[1] Department of Civil and Mechanical Engineering, Technical University of Denmark, Kongens Lyngby, Denmark

[2] Institute of Materials and Joining Technology, Otto-von-Guericke-University, Magdeburg, Germany

[3] Institute for Applied Materials, Karlsruhe Institute of Technology, Karlsruhe, Germany

[4] Ceit-BRTA, Donostia – San Sebastian, Spain

[5] Department of Physics, Technical University of Denmark, Kongens Lyngby, Denmark

*E-mail: pawo@dtu.dk

Abstract. Two metallic materials considered for the divertor in fusion reactors are manufactured by powder bed fusion through electron beam melting: tungsten as armor of plasma-facing components and an age-hardenable CuCrZr alloy as heat sink material for the divertor. Cuboids are additively manufactured from both materials, and cross sections containing the build direction are characterized by electron backscatter diffraction. A peculiar heterogeneity is observed in the microstructure of tungsten and traced to the scanning strategy. Large columnar grains along the building direction with slight outward inclination are seen on both sides of the cross section i.e. where grains are observed in viewing planes perpendicular to the printing direction. Grains appear only slightly elongated in the center; neither their entire length nor their inclination is detected when the plane of view contains the printing direction. Many incidental twin boundaries are identified in the CuCrZr alloy; their occurrence is rationalized by the presence of an almost perfect <110> fiber texture. Additionally, X-ray computed tomography confirmed the low porosity of the CuCrZr specimen.

1. Introduction

Future fusion reactors will expose plasma-facing components to high heat fluxes and only few materials will be able to withstand them [1]. Tungsten (W) is the material of choice for the armor of all plasma-facing components, while copper chromium zirconium (CuCrZr) alloys will act as heat sink material for high heat flux components and plasma-facing components in the divertor of EU-DEMO [2]. Both materials experience challenges when operating at high temperatures as deformed tungsten may recrystallize [1,3] and age-hardened CuCrZr may overage [1,4]. The present work is concerned with additively manufactured parts of both materials and peculiarities of the microstructure resulting from the manufacturing process which has to be optimized to mitigate some of the risks. Despite the advantage of additive manufacturing to produce parts with complicated geometries, only cuboidal specimens with simple geometry manufactured by powder bed fusion through electron beam melting are investigated. Electron backscatter diffraction (EBSD) and X-ray computed tomography are used to characterize the microstructure.

2. Materials and experimental techniques

2.1 Tungsten

Specimens of pure tungsten are additively manufactured by powder bed fusion via electron beam melting using a GE Additive Arcam A2X Electron Beam Melting machine at the Karlsruhe Institute of Technology [5]. Figure 1 shows the cuboidal specimen and illustrates its geometrical sizes. In each printed layer, the electron beam is scanned along nested, concentric squares as sketched in figure 1(c); the first square at the perimeter, the last one in the center of the layer. The printing directions defined in this manner can be recognized on the top surface in figure 1(a).

A 2.5 mm thick plate containing the (vertical) build direction (BD) is cut at a distance of about 3.5 mm from the outer surface (blue in figures 1(b) and 1(c)). The surface closest to the back surface is mechanically ground, polished and finally electro-polished at room temperature using an aqueous solution containing 3 wt.% NaOH with an applied voltage of 12 V and a current of approximately 2 A. Orientation data are acquired by EBSD on the entire prepared surface.
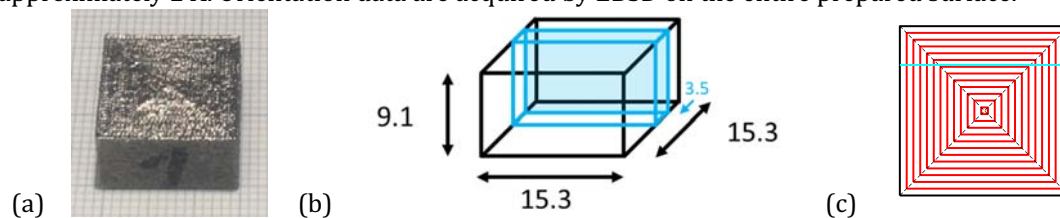

Figure 1: Additively manufactured tungsten cuboid built by electron beam melting: (a) picture of specimen on millimeter paper, (b) geometry with sketch of cutting scheme (the investigated cross section is highlighted in light blue, sizes are in millimeter), and (c) sketch of electron beam path in each layer in red.

2.2 CuCrZr

Specimens of CuCrZr are additively manufactured by powder bed fusion via electron beam melting using an adapted GE Additive Arcam Electron Beam Melting A2X device at AIDIMME Instituto Tecnológica in collaboration with Ceit [4]. Cubes with sizes $13 \times 13 \times 13$ mm^3 are printed from an alloy powder containing 0.8 wt.% Cr and 0.11 wt.% Zr obtained by gas atomization at Ceit. In each layer, the electron beam is scanned uni-directionally, i.e. along parallel lines in the same direction. The printing direction is rotated by 90° between successive layers. The powder bed temperature is set to approximately 380 °C, slightly lower than the standard ageing temperature of CuCrZr (450 °C to 475 °C). The printed cubes have a very low oxygen content in their as-build condition. Hot isostatic pressing at 400 °C and 150 MPa for 3 h reduces their porosity while the Cr precipitates are prevented to coarsen [4]. A cross section containing the build direction from the center of the cube is investigated by EBSD. Preparation of the soft CuCrZr alloy without surface damage turns out to be challenging. Following grinding and polishing, the surface is gently polished chemo-mechanically (OP-S) for 4 h to obtain a surface suitable for EBSD.

2.3 Electron backscatter diffraction

Orientation data are gathered on the prepared cross sections by electron back scatter diffraction at an accelerating voltage of 20 kV using different steps sizes. Two different scanning electron microscopes (SEMs) are used: a ZEISS Supra 35 SEM with a Nordlys EBSD detector and a ZEISS Sigma SEM using a C-Nano EBSD detector from Oxford instruments (only for a detailed map on tungsten). To gain an overview over the entire cross section of the tungsten sample, several data sets acquired from 30 smaller regions after sequential stage movements are stitched together to obtain a large orientation map. The data are analyzed using the Matlab plugin toolbox MTEX Version 5.8.2 [6] and evaluated further by own purposely developed routines.

2.4 Computed tomography

X-ray computed tomography is used to reveal internal pores in the printed CuCrZr alloy. A ZEISS Xradia 410 Versa X-ray microscope with an X-ray energy of 150 keV is utilized. For computed tomography, a slender bar-shaped specimen is cut to a size of about $1 \times 4 \times 12$ mm^3 with its long axis along the build direction and its short axis pointing from the previous outer surface into the bulk. The X-ray microscope is operated at 150 kV and 10 W using a HE1 filter and 4× objective. 2400 projections with an exposure time of 6 s per projection are acquired. Reconstruction with a voxel size of 3.54 µm^3 is achieved using a 1024×1024 camera resolution (using 2×2 binning) covering the full alloy piece within the measured volume. Image reconstruction is performed with an inbuilt acquisition and reconstruction software package (ZEISS) based on a Feldkamp, Davis and Kress algorithm with filtered back-projection [7]. The data are further analyzed and visualized using the software Avizo 3D from Thermo Fisher Scientific.

In the reconstructed volume, pores are distinguishable by their lower attenuation compared to the CuCrZr alloy. (No intensity variation attributable to precipitates are recognized.) Internal pores are identified through an intensity threshold analysis. Position, volume, and equivalent spherical diameter are determined for each individual pore.

3. Results and discussion

3.1 Armor material tungsten

Figure 2 shows a detailed orientation map obtained with a small step size of 1 µm from the center of the cross section. The two maps illustrate the presence of high angle boundaries (HABs) with disorientation angles above 15° and low angle boundaries (LABs) with disorientation angles above a certain threshold angle, but not larger than 15°. Grains can be distinguished by their different colors designating the crystallographic directions along BD or the high angle boundaries separating them. The grains appear elongated along BD and non-convex. The observed waviness of the high angle boundaries is attributed to printing layer-by-layer. The dominance of reddish and bluish colors indicates a preference for <100> and <111> directions to align with BD.
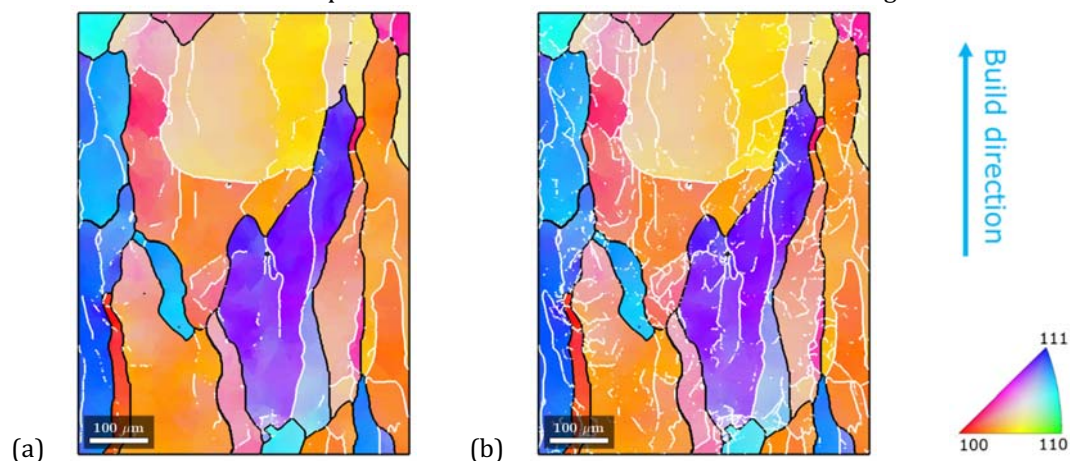

Figure 2: Orientation map obtained by EBSD in the center of the prepared cross section of a tungsten cuboid additively manufactured by electron beam melting. The colors represent the crystallographic direction along BD according to the inverse pole figure (IPF) on the right. High angle boundaries (with disorientation angles above 15°) are shown in black; low angle boundaries are marked in white for different threshold values for the disorientation angle: (a) 2° and (b) 1°.

The grains do not have a unique orientation as seen from the color variations and the presence of low angle boundaries within them. A much finer subdivision in the hierarchical structure becomes obvious in figure 2(b) when low angle boundaries with disorientation angles above 1° are shown compared to low angle boundaries above 2° in figure 2(a). From sudden changes in color apparent in the yellow-orange grain on the top of the map or the purple grain stretching almost from the bottom to the center, it becomes obvious that distinct orientation differences exist, which are resolved neither by low angle boundaries above 2°, nor such above 1°. Lowering the threshold disorientation angle for low angle boundaries even further is not advisable, as spurious artefacts appear due to the limited angular resolution of the ESBD system when acquiring orientations. Consequently, more advanced evaluation procedures (analogous to e.g. [8,9]) must be devised for characterizing the substructure within the grains in future.

The orientation map gathered from the entire cross section with a large step size of 20 μm is presented in figure 3. It illustrates the crystallographic direction along BD as well as the presence of high angle boundaries with disorientation angles above 15° and low angle boundaries with disorientation angles above 2°. All orientations of pixels indexed as tungsten are presented as collected without any filtering or removal of unindexed points (about 9 %; a higher indexing rate is preferable, but deemed unnecessary for the present purpose). The dominating red and blue colors in the entire map confirm indeed the alignment of <100> and<111> directions with BD.
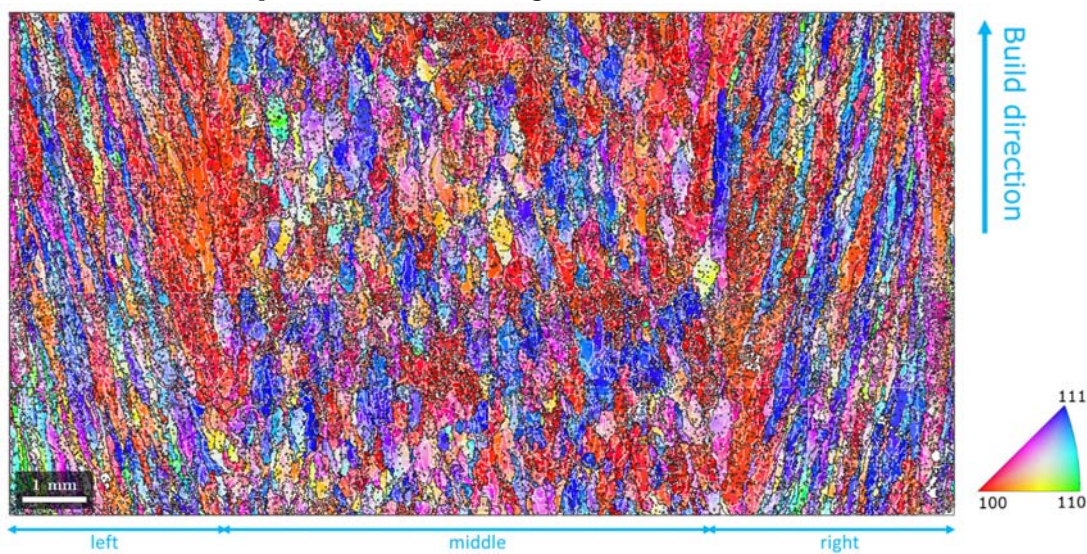

Figure 3: Orientation map obtained by EBSD on an entire cross section through a tungsten cuboid additively manufactured by electron beam melting. The colors represent the crystallographic direction along the vertical build direction according to the IPF on the right. High angle boundaries with disorientation angles larger than 15° are shown in black, low angle boundaries with disorientation angles above 2° in white. The overview map bases on 30 individual maps stitched together.

Figure 3 clearly reveals macroscopic heterogeneity in the microstructure. The entire map resembles a triptych with a central panel and two side wings. On both sides, left and right, columnar grains are inclined about 15° outwards in an opposite sense with respect to the build direction; the grains in the middle appear more equiaxed with a less, but notable elongation along the build direction. The observed outward inclination of the grains on both sides is presumably a direct consequence of the applied printing strategy within each printed layer (discussed below).

For further analysis of microstructure and texture, the entire orientation map is subdivided into three separate regions (left, middle, and right, in the manner of a triptych). For each of the three regions, the texture is analyzed individually; figure 4 shows the 100 and 111 pole figures. They confirm the preferred alignment of <100> and <111> directions with the build direction for each of the three regions, with a dominance of aligning of <100> directions over <111> directions and even similar maximal pole densities for the three regions. No fiber textures are observed; in all cases, the dominant orientation has one of its <100> directions close to the build direction and a <110> direction perpendicular to BD in the cross section as well as normal to the cross section.

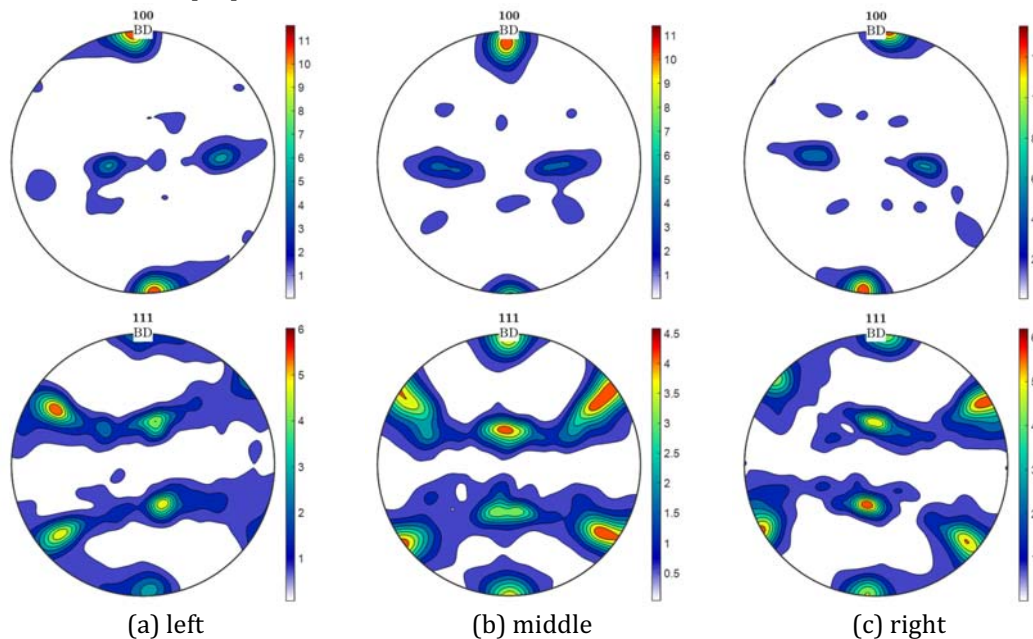(a) left   (b) middle   (c) right

Figure 4: 100 (top row) and 111 (bottom row) pole figures for three different regions on the cross section shown in figure 3 through a tungsten cuboid additively manufactured by electron beam melting.

Obviously, the textures in the three different regions are not identical and systematic tilts occur. This is most easily seen for the 100 pole figures. The 100 pole figure from the left hand side (figure 4(a)) is rotated anti-clockwise by about 6°, while the one from the right hand side (figure 4(c)) is rotated clockwise by the same amount. The 100 pole figure of the middle region in figure 4(b) is tilted 6° out of the plane of observation. All tilts and rotations are consistent with each other and the squared path of the electron beam used for printing each layer. This particular scanning scheme leads to four distinct regions in the printed cuboid separated by diagonals (see figure 1(c)). Within each region the electron beam scans on parallel paths. When printing the next layer, solidifying grains pick up an existing orientation from the layer beneath and continue to grow homo-epitaxially. As the outermost squares are printed first followed by the nested inner squares, the columnar grains become inclined perpendicular to the electron beam path. Simultaneously, the effective build direction of each columnar grain becomes slanted causing an inclination of the axis of preferred crystallographic direction. The inclination of the columnar grains, however, appears larger than that of the poles.

Scanning along nested squares causes the apparently different microstructure in the middle region of the section as well. Consequently, the grains there are also presumed to be elongated and inclined in a direction perpendicular to the mapped surface (i.e. out of plane as the 100 pole
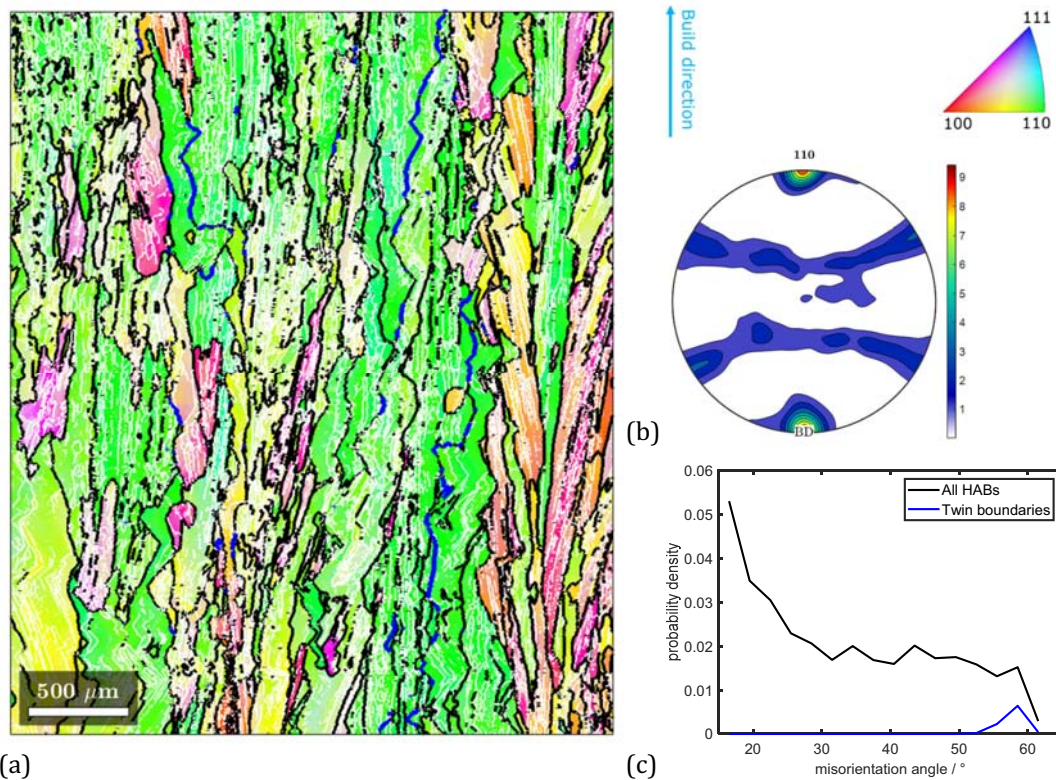
in figure 4(b)). The middle region where grains do not show any obvious inclination in the observation plane and have only a slight elongation along the build direction is about 7.7 mm wide, in good agreement with the expectation (8.3 mm) considering the section being cut at about 3.5 mm from the outer surface and subjected to some width reduction during surface preparation.

Grains are identified based on the disorientation angle between neighboring pixels as contiguous regions separated by high angle boundaries from other grains. If a grain is required to contain at least 6 pixels, the resolved grains in the entire map consist in average of 132 pixels. Only slight differences are observed for the average grain areas with some smaller grains in the middle region (129 pixels in average) compared to the left and the right (136 pixels in average). With the step size of 20 μm used for the overview map in figure 3, the average grain area becomes 52.800 $μm^2$ amounting to 18.9 grains per mm^2 corresponding to an ASTM grain size number [10] of 1.3 which is by far smaller than the ASTM grain size number of 3 or larger required for tungsten plates in the ITER materials specification [11].

3.2 Heat sink material CuCrZr
As sample preparation without surface damage is difficult for the CuCrZr alloy, the orientation data acquired on a cross section with a step size of 4 μm still contain many unindexed points (about 20%). They are removed by filtering of the data in the orientation map in figure 5(a). Columnar grains elongated along the build direction with corrugated grain boundaries dominate the microstructure. Their zigzag appearance is attributed to the layered deposition and the rotation of the scanning direction of the electron beam by 90° between the layers, cf. [4]. Both, the greenish appearance of the orientation map and the 110 pole figure in figure 5(b) reveal a strong alignment of one of the crystallographic <110> directions with the build direction; an almost perfect <110> fiber texture with only minor variations perpendicular to the build direction exists.

Several twin boundaries (as defined by their Σ3 orientation relationship) are recognized as blue lines in the orientation map of figure 5(a), in particular on the right hand side. They are neither particularly straight, nor associated with twin lamellae typical for face-centered cubic materials [12]. The occurrence of such incoherent twin boundaries between neighboring grains is purely incidental, but a direct consequence of the strong <110> fiber texture along the build direction. The Σ3 orientation relationship between twins is determined by a 60° rotation about a common <111> axis. In case of cubic symmetry, the same orientation relation can be achieved by a 72° rotation about a <110> axis. Due to the strong <110> fiber texture, most of the grains have a common <110> axis, such that the statistical occurrence of a Σ3 relationship becomes large. For an ideal <110> fiber texture with cylindrical symmetry and rotations up to 90° about the <110> axis, a rather high fraction of twin relations is expected depending on the inclination between the closest <110> direction and the fiber axis. For an average inclination angle of 5°, about 10 % of the boundaries are classified as twin boundaries according to the Brandon criterion [13], i.e. their deviation from the ideal twin relationship 60°<111> is less than 8.7°. From the distribution of disorientation angles of high angle boundaries presented in figure 5(c), a significant fraction of boundaries with disorientation angles less than 30° are observed, despite the strong <110> fiber texture. On the other hand, 2.8 % of all high angle boundaries are twin boundaries complying with the Brandon criterion; only slightly more than the 1.8 % expected for a random distribution of orientations. However, 20.6 % of all boundaries with disorientation angles above 51.3°, which possibly could be classified as twin boundaries by the Brandon criterion, are twin boundaries, compared to 9.6 % for a random orientation distribution. If only deviations less than 3° from the ideal 60°<111> rotation orientation relationship are considered as suggested in [14], even 37.8 % of all HABs with disorientation angles above 57° are classified as twin boundaries.

Figure 5: Cross section through a CuCrZr cube additively manufactured by electron beam melting: (a) orientation map obtained by ESBD with build direction vertically. The colors represent the crystallographic directions along BD according to the IPF on the right. High angle boundaries with disorientation angles larger than 15° are delineated in black, low angle boundaries above 2° in white and twin boundaries are shown as blue lines. (b) 110 pole figure with the building direction vertically. (c) boundary disorientation distribution function for all high angle boundaries, i.e. with disorientation angles larger than 15°. The contribution of twin boundaries identified according to the Brandon criterion is indicated in blue.

Reconstruction of the X-ray computed tomography data with a pixel resolution of 3.5 μm revealed 103 pores with a minimum equivalent sphere diameter of at least 4.4 μm. Figure 6(a) presents the reconstructed volume with clearly discernible pores occurring more frequently close to the former outer surface (on the left hand side in the image). The porosity amounts to a volume fraction smaller than 0.01 %. If the pore size distribution in figure 6(b) is approximated by an exponential distribution, an average pore diameter of 6.3 μm is deduced (including even the unresolved pores with equivalent sphere diameter less than 4.4 μm, i.e. with volumes smaller than the pixel size).

4. Conclusions

The microstructure and texture of pure tungsten and a CuCrZr alloy both additively manufactured by electron beam melting is characterized. In pure tungsten, a peculiar heterogeneity is observed in the microstructure of tungsten and traced to the scanning strategy of the electron beam. Large columnar grains inclined outwards are observed when grains are observed in planes perpendicular to the printing direction. In viewing planes parallel to the printing direction, grains appear only slightly elongated and neither their entire length, nor their inclination can be

observed. Many incidental twin boundaries are identified in the CuCrZr alloy which are rationalized by the development on an almost perfect <110> fiber texture. X-ray computed tomography confirms the low porosity of the CuCrZr specimen.
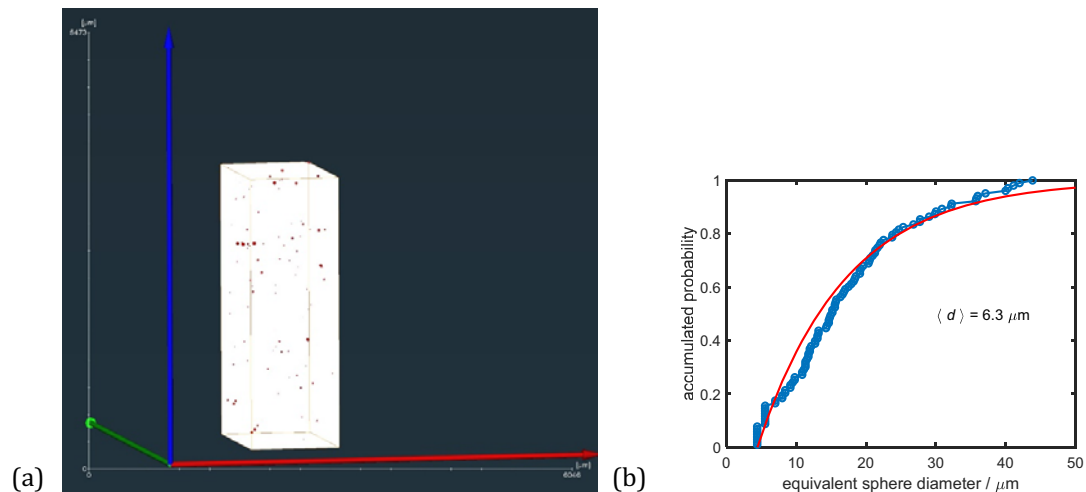

Figure 6: Results of X-ray micro computed tomography on additively manufactured CuCrZr sample: (a) reconstructed volume illustrating the spatial distribution of pores; the blue axis points along the build direction, the red axis into the specimen; the volume appears shorter along the green axis due to the used projection; the surface on the left is close to the former outer surface and (b) accumulated probability distribution of the equivalent sphere diameter of the 103 resolved pores.

Acknowledgment

References

[1]   Pintsuk G, Aiello G, Dudarev S L, Gorley M, Henry J, Richou M, Rieth M, Terentyev D and Vila R 2022 *Fus. Eng. Des.* **174** 112994:1-21

[2]   You J H et al. 2016 Fusion Eng. Des. **109-111** 1598-1603

[3]   Pantleon W 2021 *Phys. Scr.* **96** 124036:1-9

[4]   Ordás N, Portolés L, Azpeleta M, Gómez A, Blasco J R, Martinez M, Ureña J and Iturriza I 2021 *J. Nucl. Mater.* **548** 152841:1-9

[5]   Antusch S et al. 2024 *Nucl. Mater. Energy* **39** 101683:1-24

[6]   Bachmann F, Hielscher R and Schaeben H 2010 *Solid State Phenom.* **160** 63-68

[7]   Feldkamp L A, Davis L C and Kress J W 1984 *J. Opt. Soc. Am.* **1** 612-619

[8]   Pantleon W 2005 *Mater. Sci. Techn.* **21** 1392-1396

[9]   Pantleon W, He W, Johansson T P and Gundlach C 2008 *Mater. Sci. Eng. A* **483-484** 668-671

[10]   ASTM E112-13 2013 Standard Test Methods for Determining Average Grain Size

[11]   Hirai T et al. 2016 *Nucl. Mater. Energy* **9** 616-622

[12]   Alimadadi H, Fanta A B, Somers M A J and Pantleon K 2014 *Surf. Coat. Techn.* **254** 207-216

[13]   Brandon D G 1966 *Acta Metall.* **14** 1479-1484

[14]   Mishin O V and Huang X 1999 *Mater. Sci. Forum* **294-296** 401-404